



ELSEVIER

Available online at www.sciencedirect.com

ScienceDirect

Proceedings of the Combustion Institute xxx (2014) xxx–xxx

Proceedings
of the
Combustion
Institutewww.elsevier.com/locate/proci

Quantitative infrared imaging of impinging turbulent buoyant diffusion flames

Ashish S. Newale^{a,c,*}, Brent A. Rankin^{a,d}, Harshad U. Lalit^b,
Jay P. Gore^a, Randall J. McDermott^e

^a School of Mechanical Engineering, Purdue University, West Lafayette, IN 47907, USA

^b School of Aeronautics and Astronautics, Purdue University, West Lafayette, IN 47907, USA

^c CD-adapco, Houston, TX 77042, USA

^d Innovative Scientific Solutions Inc., Dayton, OH 45459, USA

^e Fire Research Division, National Institute of Standards and Technology, Gaithersburg, MD 20899, USA

Abstract

A buoyant fire impinging on a horizontal ceiling at a certain distance from the fuel source occurs in many practical fire scenarios. Motivated by this application, infrared radiation from buoyant diffusion flames with and without impingement on a flat plate is studied using a quantitative comparison of measured and simulated images. The measured quantitative images of the radiation intensity are acquired using a calibrated high speed camera. Simulated radiation intensities are rendered in the form of images and compared quantitatively with the measured images. The simulated radiation intensities are obtained using the radiative transfer equation with local absorption coefficients evaluated using a narrowband radiation model. The instantaneous local species concentrations, soot volume fractions, and temperatures necessary for these simulations are calculated using the Fire Dynamics Simulator (FDS) version 6. The measured images reveal that the characteristic necking and bulging ($7 \text{ Hz} \pm 1 \text{ Hz}$) of the free buoyant flame is suppressed to a large extent by impingement on the plate. The roll-up vortices in the impinging flame are much smaller than those in the free flame. The stagnation point boundary layer inferred from the computed images is thicker at some instances than that inferred from the measurements. Qualitative and quantitative comparisons between the measured and computed infrared images for both the free and the impinging fires reveal many similarities as well as differences useful for model evaluation.

© 2014 The Combustion Institute. Published by Elsevier Inc. All rights reserved.

Keywords: Turbulent buoyant flames; Impinging flames; Flame radiation; Fire Dynamics Simulator; Infrared imaging

1. Introduction

Fire structure interaction studies explore the complex interactions between the gas phase flow field and heat release rate and the structural and thermal properties of load bearing elements. In particular, a buoyant fire impinging on a

* Corresponding author. Address: CD-adapco 11000 Richmond Avenue, Suite 110, Houston, TX 77042, USA.

E-mail address: ashish.newale@gmail.com (A.S. Newale).

<http://dx.doi.org/10.1016/j.proci.2014.05.115>

1540-7489/© 2014 The Combustion Institute. Published by Elsevier Inc. All rights reserved.

Nomenclature

n	unit normal vector on the cell face	C_c	empirical coefficient for natural convection
s'	direction vector of the radiation intensity	C_r	corrective factor for radiative loss term
dV	cell volume	h	heat transfer coefficient
\dot{q}'''	heat release rate per unit volume	I	radiation intensity
\dot{q}_c''	convective heat flux	κ	absorption coefficient
$I_{b\lambda}$	spectral black body radiation intensity	κ_λ	spectral absorption coefficient
k	thermal conductivity	λ_1, λ_2	filter bandwidth limits
L	characteristic length	Ω	solid angle
Nu	Nusselt number	σ	Stefan–Boltzman constant
Pr	Prandtl number	τ_λ	spectral optical thickness
Re	Reynolds number	ε	emissivity
s	pathlength through flame		
T	temperature		
t	time		
U	integrated radiation intensity		
		<i>Subscripts</i>	
		g	gas
		ijk	gas phase cell indices
		s	solid
		w	wall
<i>Greek symbols</i>			
χ_r	radiative heat loss fraction		
\dot{q}_r''	radiative heat flux		

horizontal ceiling at a certain distance from the fuel source occurs in many practical fire scenarios. Heat transfer from a fire to a structure has been the subject of many investigations [1–3]. Radiation and convection heat transfer have been established as important modes of energy transfer between the gas phase and the solid [4]. Trouvé and Wang [5] suggested that comparing higher order statistics resulting from measurements and simulations of fires is an important direction for advancing progress within the fire modeling field. The current work involves a comparison of time-dependent images and higher order statistics of infrared radiation intensity from non-impinging and impinging buoyant diffusion flames.

One of the most challenging aspects of coupled fire structure interaction simulations is the significant range in the time and length scales. The different numerical methods used for fire, thermal, and structural simulations lead to difficulties in determining an efficient method of transferring information between these simulations [4]. Weng and Hasemi [1] developed an analytical model to determine the thermal response of an unconfined non-burning ceiling to an impinging buoyant diffusion flame. The model showed good agreement with experimental heat flux data in regions far from the stagnation point. You [6] developed an integral model for impinging turbulent buoyant diffusion flames to determine mean velocities, temperature and major species concentrations in the plume region. The integral model was extended to the ceiling jet region and provided good agreement with measured velocities and heat fluxes [2]. Tuttle

et al. [7,8] reported time-dependent and time-averaged measurements of axial and radial profiles of local heat fluxes from partially premixed methane-air flames impinging on a water-cooled plate. The coupling between flame structure and heat transfer was explored by qualitatively correlating visible photographs of the flame to measured heat flux profiles. Premixed flames typically produce the highest heat flux and are used in industrial applications to provide localized heat transfer. Baukal and Gebhart [9] and Viskanta [10] have reported comprehensive reviews on flame impingement heat transfer for manufacturing applications.

A quantitative comparison of measured and computed images of radiation intensity is an effective method for prompting improvements in combustion and radiation models [11]. Rankin et al. [12,13] measured and computed quantitative images of infrared radiation intensity from a representative turbulent non-premixed jet flame from the International Workshop on Measurement and Computation of Turbulent Nonpremixed Flames. The computed images utilized scalar results from large-eddy simulations (LES) of the flame performed by Ihme et al. [14]. The measured and computed radiation intensities agreed to within approximately 20% for regions upstream of the stoichiometric flame length. Differences between the measured and computed radiation intensities near and downstream of the stoichiometric flame length suggested that including radiation heat loss effects in the simulations is important even for weakly radiating flames.

Motivated by a review of existing literature on fire-structure interactions and the potential of

computational and experimental quantitative infrared imaging techniques, the specific objectives of the current study are:

- (1) Measure quantitative images of the narrow-band infrared radiation intensity from a representative buoyant diffusion flame with and without impingement on a stagnation plate.
- (2) Compute images of the narrowband infrared radiation intensity using time dependent fire simulations, a narrowband radiation model, and the radiative transfer equation.
- (3) Study the effects of flame impingement on flame radiation by comparing the measured and computed images.
- (4) Compare measured and computed mean, root mean square (RMS), and power spectral densities (PSDs) of the radiation intensity.

The measurements reveal a less prominent peak at a characteristic frequency of 7 Hz for the impinging buoyant diffusion flame compared to the non-impinging flame. The roll-up vortices in the impinging flame are much smaller than those in the free flame. The stagnation point boundary layer inferred from the computed images is thicker at some instances than that inferred from the measurements. The quantitative comparative study of measured and computed images suggests the need for radiation and combustion model improvements.

2. Experimental methods

2.1. Turbulent buoyant diffusion flame

A turbulent buoyant diffusion flame is established on a diffuser burner [15] with an exit diameter of 7.1 cm. The diverging angle of the burner is 7° such that the gaseous fuel (methane) is decelerated and forms close to a uniform velocity distribution at the burner exit. The methane (CH₄) mass flow rate (84.3 mg/s ± 3%) is calibrated using a dry test turbine meter and controlled by setting the pressure upstream of a choked orifice plate. Measured and computed vertical and horizontal velocity, mixture fraction, and temperature values for this flame have been reported by Zhou and Gore [15] and Xin et al. [16].

A schematic of the experimental arrangement and coordinate system definitions for the radiation measurements are illustrated in Fig. 1. A square steel plate (25.4 cm × 25.4 cm × 0.254 cm) is oriented perpendicular to the flame centerline and suspended at an axial location of 14.2 cm ($Z/D = 2$) downstream of the burner exit. The plate is supported at each of the four corners on

the bottom surface using thin brackets to minimize flame disturbance.

2.2. Radiation intensity measurements

Time dependent images of the radiation intensity from the flame and the plate are measured using a calibrated infrared camera with a 25 mm lens ($f/2.3$) and an indium antimonide (InSb) detector. A narrowband filter ($2.77 \mu\text{m} \pm 0.12 \mu\text{m}$) is used to measure the radiation intensity originating from water vapor, carbon dioxide, and soot. The spatial resolution of the radiation intensity measurements is approximately 0.97 mm for each pixel at the center of the flame. The infrared camera sampling frequency is 330 Hz and the exposure time is 10 s. The experimental uncertainty in the mean and RMS radiation intensity for diametric paths is estimated to be less than ±15% based on three repeated measurements of a turbulent jet diffusion flame using the same infrared camera and optical arrangement [12].

3. Computational methods

3.1. Scalar computations

Fire Dynamics Simulator (FDS) version 6 is used to simulate the turbulent buoyant diffusion flame with and without impingement. FDS is a large eddy simulation (LES) code based on a set of governing equations for low-Mach number flows [17]. For the calculations presented in this paper, the LES subgrid closures are based on the dynamic Smagorinsky model [18] with constant turbulent Schmidt and Prandtl numbers. The mean chemical source term is closed using the eddy dissipation concept [19].

The computational domain for the flame without impingement is 20 cm × 20 cm × 40 cm. The computational domain used for the impinging flame simulation is 30 cm × 30 cm × 22 cm. A uniform grid with 4 mm spatial resolution is used for both the non-impinging and impinging flame simulations. A radiative heat loss fraction of 10% is specified for both flames based on past estimates [16]. The radiative loss term is computed in each cell with the gray gas assumption as a product of blackbody radiation intensity and a corrective factor, C_r [17] as defined below:

$$C_r = \frac{\sum_{\dot{q}_{ijk}''' > 0} (\chi_r \dot{q}_{ijk}''' + \kappa_{ijk} U_{ijk}) dV}{\sum_{\dot{q}_{ijk}''' > 0} (4 \kappa_{ijk} \sigma T_{ijk}^4) dV}. \quad (1)$$

The corrective factor is set to dynamically ensure that the global integral of the product of radiative heat loss fraction and heat release rate is satisfied.

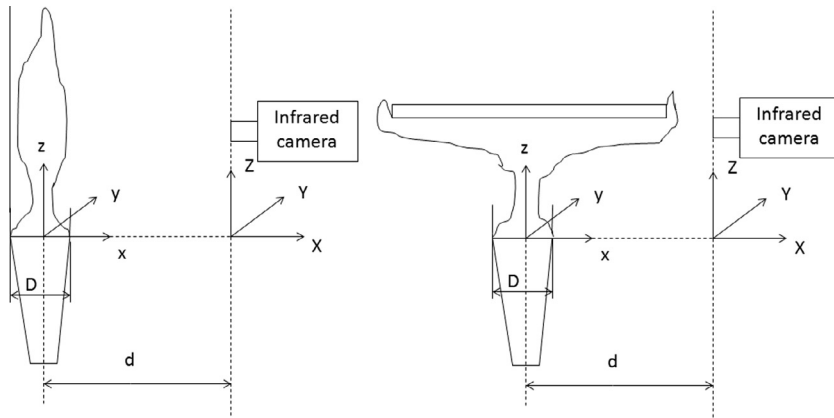


Fig. 1. A schematic of the experimental arrangement for radiation intensity imaging measurements of the turbulent buoyant diffusion flames without (left) and with (right) impingement on a stagnation plate. Note that $D = 7.1$ cm and $d = 80$ cm.

The boundary conditions at the burner exit plane are defined to be a uniform axial velocity and fuel mass fraction profiles ($w = 3.14$ cm/s, $Y_F = 1$). Open boundary conditions are specified for the remaining bounding surfaces of the computational domain. The plate is specified as conducting and heat transfer occurs from both the flame and wake sides of the plate. The initial temperature of the plate is specified to be equal to ambient conditions. The boundary conditions on both the front and back surfaces of the plate are implemented [17] as follows:

$$-k_s \frac{\partial T_s}{\partial x}(0, t) = \dot{q}''_c + \dot{q}''_r. \quad (2)$$

The convective heat flux and convection heat transfer coefficients are computed as,

$$\dot{q}''_c = h(T_g - T_w); \quad h = \max \left[C_c |T_g - T_w|^{\frac{1}{4}}, \frac{k}{L} Nu \right], \quad (3)$$

where C_c is specified as 1.52 for a horizontal plate and L is specified as 1 m. The Nusselt number is computed as,

$$Nu = 0.037 Re^{0.8} Pr^{0.33}. \quad (4)$$

The radiative heat flux is computed as follows:

$$\dot{q}''_r = \varepsilon \int_{s' \cdot \mathbf{n}_w < 0} I_w(s') |s' \cdot \mathbf{n}_w| d\Omega - \varepsilon \sigma T_w^4. \quad (5)$$

3.2. Radiation intensity computations

Computed images of the radiation intensity from the flames are rendered using the computed scalar values, a narrowband radiation model and the radiative transfer equation with a customized in-house code. The narrowband radiation

intensity (I) emitted from parallel lines-of-sight through the flame is computed using the solution of the radiative transfer equation for non-scattering media [20], with the addition [11–13] of a spectral coefficient (α_i) associated with the transmission optics and spectral integration over the band-pass filter,

$$I = \int_{\lambda_1}^{\lambda_2} \alpha_i I_i(0) e^{-\tau_\lambda} d\lambda + \int_{\lambda_1}^{\lambda_2} \int_0^{\tau_\lambda} \alpha_i I_{b\lambda}(\tau_\lambda^*) e^{-(\tau_\lambda + \tau_\lambda^*)} d\tau_\lambda^* d\lambda. \quad (6)$$

The spectral optical thickness is defined as:

$$\tau_\lambda = \int_0^s \kappa_\lambda ds. \quad (7)$$

The spectral absorption coefficient (κ_λ) is calculated using the computed scalar values and a narrowband radiation model [21]. The intensity is calculated by integrating along lines-of-sight through the flame, applying the spectral response of the optics and camera, and integrating over the spectral range of the filter to allow for comparison with the measured values. An image of the radiation intensity from the flames is obtained by performing the radiation intensity computations along multiple parallel lines-of-sight through the flame consistent with the spatial and temporal resolution of the computed scalar values.

The images of the radiation intensity are calculated starting at 10 s to exclude initial transients in the simulations. Time intervals of 10–20 s with a sampling frequency of 33 Hz are sufficient to obtain statistically stationary mean values of the radiation intensity. The higher order statistics are calculated over a time interval of 10–40 s with a sampling frequency of 200 Hz.

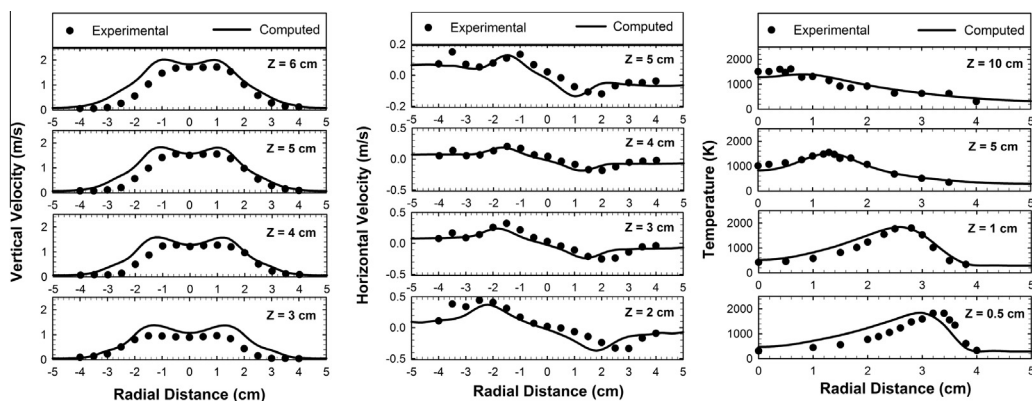


Fig. 2. Measured [15] and computed radial profiles of the mean vertical velocity (left), horizontal velocity (center), and temperature (right) at select heights above the burner exit.

4. Results and discussion

Figure 2 shows a comparison of the radial profiles of vertical velocity, horizontal velocity, and temperature from the current computation of the non-impinging flame with previous measurements reported by Zhou and Gore [15]. These past measurements extend to the distance of 10 cm downstream of the burner exit compared to approximately 22 cm for the current radiation intensity measurements. The radial profiles for temperature reported by Zhou and Gore [15] and Xin et al. [16] were estimated from species concentration measurements assuming an adiabatic flame. The measured and computed vertical velocities agree to within approximately 15% along the flame centerline. The locations of the peak magnitude of the vertical and horizontal velocities observed in the measurements and computations agree to within approximately 1 cm. The results of the computations agree with the experimentally derived temperature profiles within 15% beyond 0.5 cm downstream of the burner exit.

Figure 3 compares six instantaneous temporally related realizations of radiation intensity images obtained from the measurements and the computations for the non-impinging buoyant diffusion flame. The six realizations encompass one pulsation cycle. The instantaneous realizations of time-dependent radiation intensity images are separated by an interval of 30 ms. The initial phase in the pulsation cycle is matched for measurements (top six panels) and computations (bottom six panels). The peak magnitude of radiation intensity observed in the measurements ($500 \text{ W/m}^2\text{-sr}$) is captured by the computations in each of the six panels comprising one realization of the pulsation cycle. The remarkable dynamic range ($0 \text{ W/m}^2\text{-sr}$ to $500 \text{ W/m}^2\text{-sr}$) illustrated by the measurements is matched by the computations. It is remarkable

that the identical range and increment used in the rendering color palette leads to many similarities in the observed patterns. For example, the left most measured and computed images both show a concentric conical flame attachment region followed by necking and formation of a bulging structure with two symmetric red circles corresponding to the high temperature region associated with the buoyant vortex ring. This agreement approximately repeats itself in every sixth image as shown in the right most images of the top and the bottom panels. However, there are specific differences in the degree of spatial organization between the measured and the computed images in each of the six interim phase panels. In particular, the measured intensities show significantly higher symmetric organization compared to the computed intensities. For example, the highest intensities depict a continuation of a symmetric bulging shape in the measured image of the second top panel while the highest intensities show a dislocation of the left part of the bulging shape by apparent faster advection and expansion in the computed image of the second bottom panel. These processes result in an L-shaped structure with the two highest intensity circles appearing at each end in the computed image. Similar distortions exist in each one of the four intermediate phase panels in the top and bottom rows of Fig. 3. While similar differences each with their own aesthetic but unimportant individuality exist throughout the measured and simulated images, the net result is of significantly larger disorganization in the simulated compared to the measured cycles. These observations may be of value for continuous improvements in aspects of fire dynamics simulations not discussed here for brevity with interested readers referred to the FDS documentation [17].

Figure 4 shows a comparison of six time-dependent radiation intensity images for the impinging

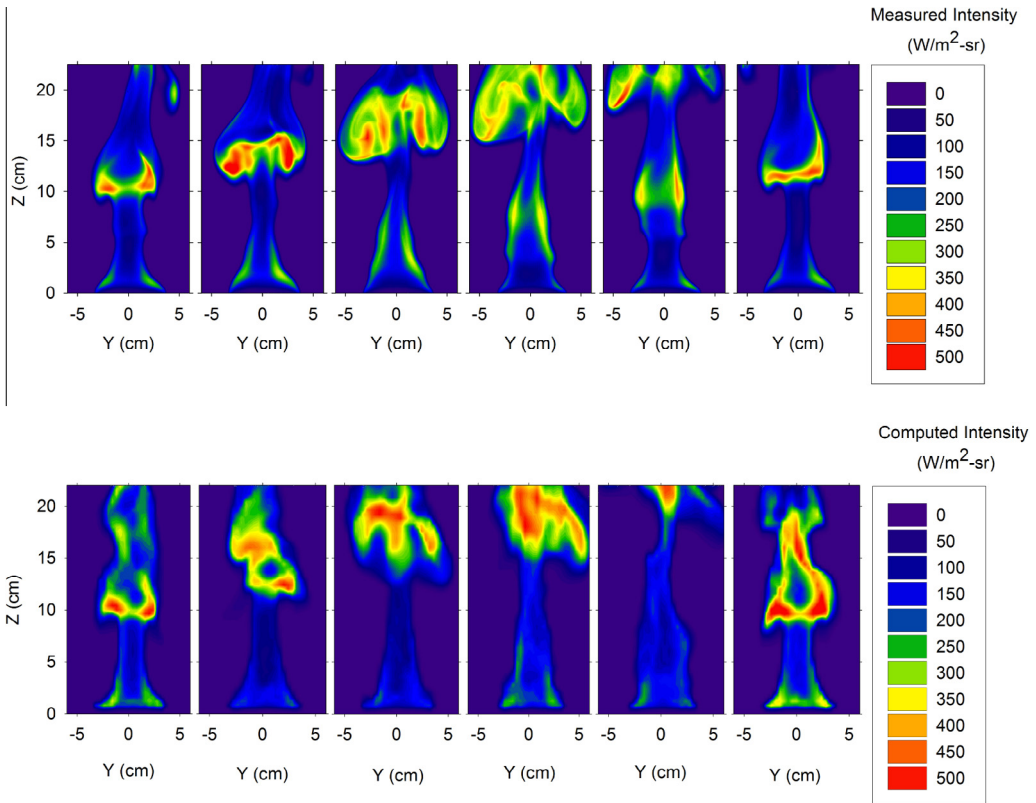


Fig. 3. Measured (top) and computed (bottom) time-dependent images of the radiation intensity from the non-impinging turbulent buoyant diffusion flame (characteristic puffing mode frequency is 7 Hz).

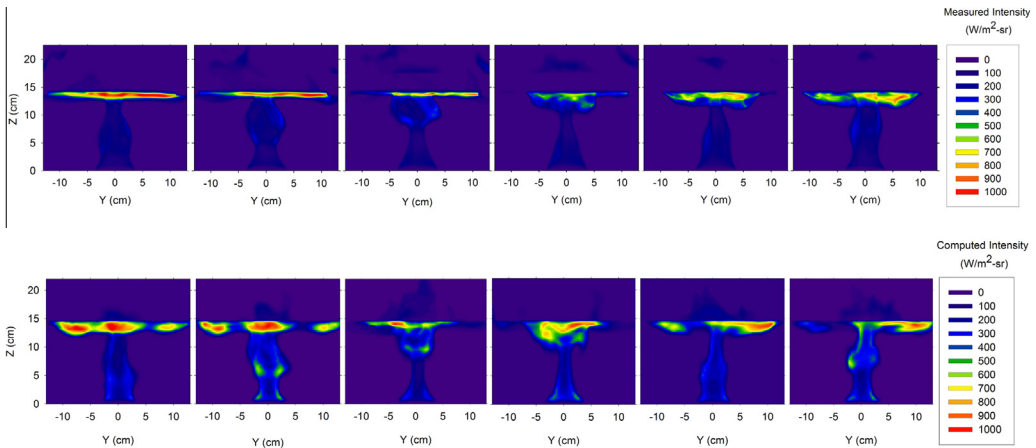


Fig. 4. Measured (top) and computed (bottom) time-dependent images of the radiation intensity from the turbulent buoyant diffusion flame impinging on the plate suspended at $Z = 14.2$ cm.

flame. Six images are shown as before to encompass one pulsation cycle and the initial phase in the pulsation cycle is matched between measurement and computations. The time-dependent images show a region of high radiation intensity

at small distances upstream of the plate. The computations capture the peak magnitude of radiation intensity observed in the measurements ($1000 \text{ W/m}^2\text{-sr}$). The peak magnitude observed for the impinging flame is twice that for the

non-impinging flame partially because of the increased path length through the stagnation point boundary layer. Very strong stabilizing effects of the flow stagnation are apparent in the experimental images. The computed intensity images continue to show remnants of the axially symmetric vortex structure in most panels in the bottom half of Fig. 4. This qualitative observation is confirmed by comparisons of measured and computed power spectral densities discussed later in the paper. The third and the fourth measured and computed images in the cycle show impingement of the vortex structure on the stagnation plate. The apparent high intensity region of the measured structure is twice as thick as that of the computed structure. Measured and computed instantaneous images of the infrared radiation intensity from the free and impinging buoyant diffusion flames are rendered in the form of animations and provided as supplementary material. Further quantitative comparisons of the effects rendered in the instantaneous images shown in Figs. 3 and 4 are studied in Figs. 5 and 6.

Figure 5a shows the measured and computed mean radiation intensities from diametric paths as function of distance downstream of the burner exit for the non-impinging and the impinging flames. The measurements and the computations beyond approximately 4 cm downstream of the burner exit are within 25% of each other. The factor of two differences between the computed and measured mean and fluctuating radiation intensity near the burner exit exist because of relatively simple models of the burner exit boundary conditions including partial premixing, heat loss, and finite rate chemistry. It is remarkable that the mean radiation intensities are dominated by the buoyancy induced advection and mixing overcoming the effects of boundary conditions. Both the measurements and the computations show that the

peak magnitude of the mean radiation intensity for the impinging flame occurs at approximately 0.5 cm upstream of the stagnation point. This is consistent with the relatively short duration exposure of the relatively cold plate to the impinging flame. The differences in the sharp peak value of the intensity may be addressed by future enhancements in the stagnation point combustion model. The location of the peak magnitude of mean radiation intensity for the impinging flame is also indicative of the upstream propagation effect of the plate on the buoyant diffusion flame. Measured and computed time-averaged images of the infrared radiation intensity from the free and impinging buoyant diffusion flames are provided as supplementary material.

The root mean square (RMS) values of radiation intensity from diametric paths normalized by the mean radiation intensity are plotted as a function of distance downstream of the burner exit in Fig. 5b. The measured and computed normalized RMS increase downstream of the burner exit region for both the impinging and the non-impinging flames. The measured and computed normalized RMS profiles of radiation intensity for the impinging flame show a local minimum at approximately 0.5 cm upstream of the stagnation point caused by the stabilizing effects of the stagnation point boundary layer.

Figure 6 shows a comparison of the measured and computed power spectral density (PSD) of radiation intensity from diametric paths for the non-impinging and impinging buoyant diffusion flames at a location selected to correspond to the measured peak mean intensity ($Y = 0$ cm, $Z = 13.6$ cm) for the impinging flame. The measured and computed PSDs shown in the left panel depict the expected peaks at pulsation frequencies of approximately 7 Hz and the expected decrement according to a power law at frequencies

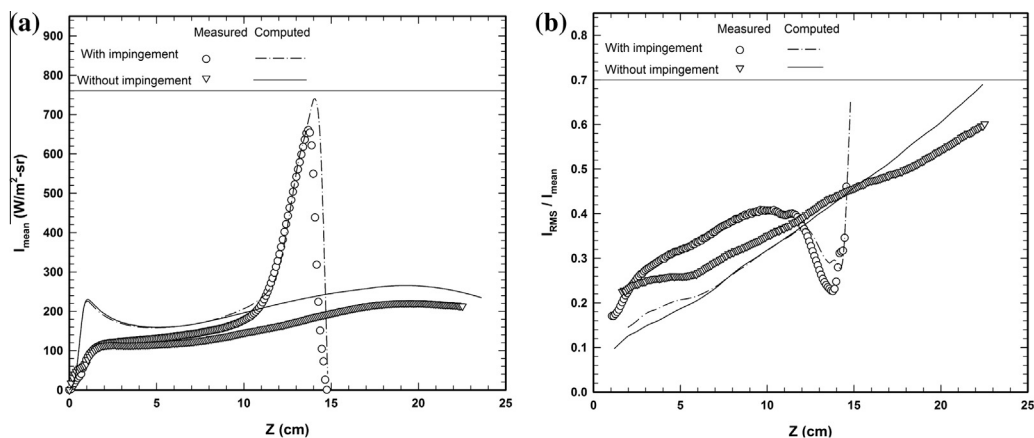


Fig. 5. Measured and computed mean (a) and normalized root mean square (RMS) (b) of the radiation intensity emitted from diametric paths ($Y = 0$ cm) as a function of distance downstream of the burner exit.

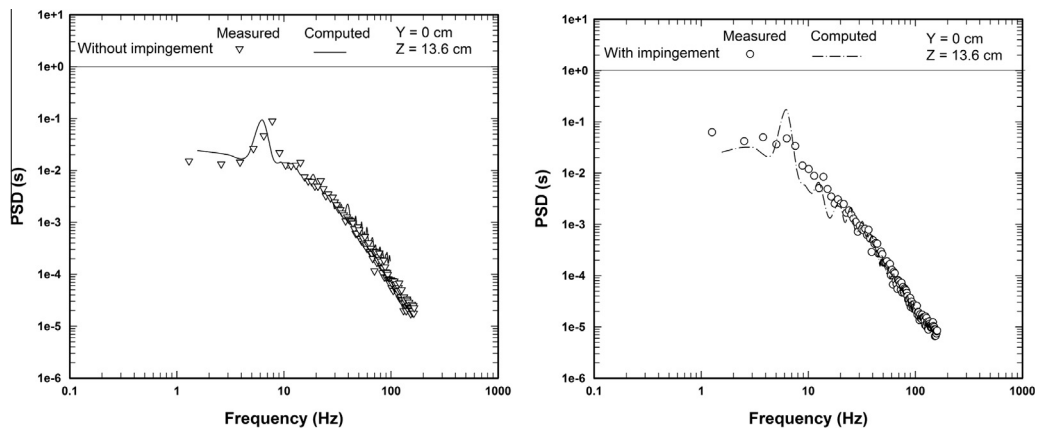


Fig. 6. Measured and computed power spectral density (PSD) functions for the non-impinging (left) and impinging (right) buoyant diffusion flames at a select location.

higher than 10 Hz. The measured PSD in the right hand panel of Fig. 6 show that a less prominent peak is observed at the characteristic frequency of 7 Hz compared to the non-impinging flame. This can be attributed to the pressure gradient introduced by the stagnation point boundary layer. This drop in magnitude of the PSD at the pulsation frequency is consistent with the reduced RMS of intensity and underlying temperature and scalar fluctuations resulting from the effects of the stagnation point. This experimental observation is not only of significant practical relevance for example in fire sensing but also may prompt future improvements in fire simulations.

5. Conclusions

A quantitative comparative study of measured and computed images of the radiation intensity from non-impinging and impinging turbulent buoyant diffusion flames is utilized to evaluate fire dynamic simulations. The computed mean radiation intensities agree with the measurements to within 20 % downstream of the flame stabilization region. The computed images of the radiation intensity capture the flame necking and bulging of the non-impinging flames observed in the measurements.

The pressure gradient introduced by the stagnation point boundary layer leads to significant smoothing of the PSD near the characteristic frequency (7 Hz) of the buoyant diffusion flame. The roll-up vortices in the impinging flame are much smaller than those in the free flame. The stagnation point boundary layer inferred from the computed images is thicker at some instances than that inferred from the measurements. Qualitative and quantitative comparisons between the measured and computed infrared images for both

the free and the impinging fires reveal many similarities as well as differences useful for model evaluation.

Acknowledgements

The National Institute of Standards and Technology and the National Science Foundation are gratefully acknowledged for supporting previous flame structure interaction work at Purdue University. The authors thank Dr. Matthias Ihme for insightful technical discussions.

Appendix A. Supplementary data

Supplementary data associated with this article can be found, in the online version, at <http://dx.doi.org/10.1016/j.proci.2014.05.115>.

References

- [1] W. Weng, Y. Hasemi, *Heat Mass Transfer* 42 (2006) 652–659.
- [2] H. You, *Fire Mater.* 9 (1985) 46–56.
- [3] H. You, G. Faeth, *Fire Mater.* 3 (1979) 140–147.
- [4] H. Baum, *Mech. Res. Commun.* 38 (2011) 1–11.
- [5] A. Trouvé, Y. Wang, *Int. J. Comput. Fluid Dynam.* 24 (2010) 449–466.
- [6] H. You, *Fire Mater.* 8 (1984) 28–39.
- [7] S. Tuttle, B. Webb, M. McQuay, *Int. J. Heat Mass Transfer* 48 (2005) 1236–1251.
- [8] S. Tuttle, B. Webb, M. McQuay, *Int. J. Heat Mass Transfer* 48 (2005) 1252–1266.
- [9] C. Baukal, B. Gebhart, *Combustion Sci. Technol.* 104 (1995) 339–357.
- [10] R. Viskanta, *Exp. Therm. Fluid Sci.* 6 (1993) 111–134.

- [11] B. Rankin, D. Blunck, V. Katta, S. Stouffer, J. Gore, *Combustion Flame* 159 (2012) 2841–2843.
- [12] B. Rankin, Quantitative Experimental and Model-based Imaging of Infrared Radiation Intensity from Turbulent Reacting Flows, Ph.D. thesis, Purdue University, West Lafayette, IN, USA, 2012.
- [13] B. Rankin, D. Blunck, J. Gore, *J. Heat Transfer* 135 (2013).
- [14] M. Ihme, H. Pitsch, D. Bodony, *Proc. Combustion Inst.* 32 (2009) 1545–1553.
- [15] X. Zhou, J. Gore, *Proc. Combustion Inst.* 27 (1998) 2767–2773.
- [16] Y. Xin, J. Gore, K. McGrattan, R. Rehm, H. Baum, *Combustion Flame* 141 (2005) 329–335.
- [17] Fire Dynamics Simulator, Technical Reference Guide, National Institute of Standards and Technology, Gaithersburg, Maryland, USA and VTT Technical Research Centre of Finland, Espoo, Finland, sixth ed., 2013.
- [18] P. Moin, K. Squires, W. Cabot, S. Lee, *Phys. Fluids* 3 (1991) 2746–2757.
- [19] B. Magnussen, B. Hjertager, *Proc. Combustion Inst.* 16 (1977) 719–729.
- [20] M. Modest, *Radiative Heat Transfer*, McGraw-Hill Inc., New York, 2003.
- [21] W. Grosshandler, RADCAL: A Narrow-band Model for Radiation Calculations in a Combustion Environment, National Institute of Standards and Technology, 2005.